On the Spatial Resolution of Fault Location Techniques Based on Full Fault Transients

Shao-Yin He, Andréa Cozza, Yan-Zhao Xie

On the Spatial Resolution of Fault Location Techniques Based on Full Fault Transients

Shao-yin He, Andrea Cozza, *Senior Member, IEEE*, Yan-zhao Xie, *Senior Member, IEEE*

***Abstract*—This paper discusses the mechanisms enabling spatial resolution in fault location methods based on full transient signals, as opposed to those only using their early-time portion. This idea is found in recent travelling-wave methods (TWM) and those based on electromagnetic time reversal (EMTR). Their spatial resolution is discussed in terms of the sensitivity of a system resonances to change in the fault position and their coherence bandwidth. It is proven that using the entire transient signal it is possible to bypass the Fourier transform uncertainty principle, which limits the spatial resolution of time-domain reflectometry and standard early-time TWM. Super-resolved fault location is shown to be possible only for resonating systems, enabling high spatial resolution without relying on wide-band data. A detailed theoretical analysis for laterals and numerical results for networks and a three-phase line show that significant differences can be observed for the spatial resolution associated to each resonance, most often resulting in a loss of spatial resolution. The interaction between separate resonant structures, such as laterals in networks and coupled conductors in three-phase lines are shown to be main cause of resolution loss.**

***Index Terms*—Fault location, fault transients, spatial resolution, power grids, correlation methods, characteristic frequencies.**

I. Introduction

TRAVELLING-WAVE methods (TWM) have been developed over the years to provide accurate fault location, by processing fault transient signals, e.g., the voltage $v_m(t)$ recorded by a probe, usually placed at the end of a line, e.g., at the busbar of a power transformer, resulting from the initial fault surge $v_f(t)$ propagating away from the fault [1]–[3], as schematically depicted in Fig. 1. They basically operate as time-domain reflectometry methods, exploiting the fault surge signal $v_f(t)$ itself to estimate the fault distance [4], e.g., by measuring the propagation delay between the first observation of the fault surge and subsequent reflections over the fault. To do so, TWM need to separate impinging and reflected portions of the fault transient signal, which may require relatively large bandwidths, potentially a drawback, but also the reason behind their good spatial resolution.

Alternative formulations of TWM that dispense with signal separation were more recently discussed in [5]–[7], where the series of multiple echoes appearing in the full fault transient is regarded as accurately and uniquely encoding the distance L from the probe at which the fault occurs, an idea also discussed in [8]. Decoding the fault position from its transient is based on the assumption that reference results be available, typically transients $\hat{v}_m(t;\hat{L})$ that would be generated by faults at an arbitrary position $\hat{L}$. The fault position is then estimated, e.g., as the one presenting the highest correlation $\rho(\hat{L})$ between measured and simulated fault transient signals, which can be expressed as follows

$$\rho(\hat{L}) = \left(A_m(L)A_m(\hat{L})\right)^{-1} \int \mathrm{d}t\, v_m(t)\hat{v}_m(t;\hat{L}) \qquad (1)$$

with $A_m(L)$ and $A_m(\hat{L})$ the L_2 norms of $v_m(t)$ and $\hat{v}_m(t;\hat{L})$, respectively. A similar approach to fault location is found in the recent proposal of using ElectroMagnetic Time Reversal (EMTR), where a fault transient signal is re-injected into a numerical model of the line, and the fault located by monitoring where it focuses back with the highest intensity [9]. As proven in [10], EMTR operates by approximating a correlation.

Assuming the availability of propagation models for the line or network (e.g., numerical or theoretical) is clearly a critical issue and requires a careful assessment of the robustness of the results to tolerances in the system parameters, such as termination loads and propagation losses. Empirical evidence supporting robustness can be found in [5], [9], [11], [12], but a general analysis is not available in the literature, to the best of our knowledge.

Parseval theorem allows to recast (1) in terms of Fourier spectra, now implying that the fault position is found by identifying its transient spectrum. A similar viewpoint, though mostly restricted to single lines rather than networks, is adopted in papers analyzing the characteristic frequencies of the fault transient [13]–[15], representing the natural resonant

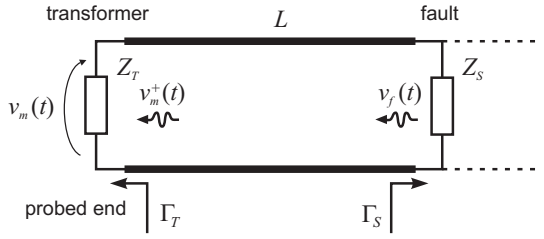

Fig. 1. Single-phase line with shunt fault at a distance L from its probed end, generating a surge voltage $v_f(t)$, giving rise to a voltage wave $v_m^+(t)$ impinging on the probe and the recorded voltage transient $v_m(t)$.

(Corresponding author : A. Cozza.).
This work was partially supported by the National Natural Science Foundation of China under Grant 51677148.
S.-Y. He, Y.-Z. Xie, are with the State Key Laboratory of Electrical Insulation and Power Equipment, School of Electrical Engineering, Xi'an Jiaotong University, Xi'an 710049, China (email: shaoyin.he@xjtu.edu.cn; yzxie@xjtu.edu.cn).
A. Cozza is with the Group of Electrical Engineering - Paris (GeePs), CentraleSupelec, Univ. Paris-Sud, Université Paris-Saclay, Sorbonne Universites, UPMC Univ Paris 06, 3 & 11 rue Joliot-Curie, Plateau de Moulon 91192 Gif-sur-Yvette CEDEX, France (email: andrea.cozza@ieee.org).

frequencies of a line where the fault occurs. By estimating these frequencies it is possible to infer the fault distance, again assuming an accurate knowledge of the the line characteristics.

Because all these methods rely on an assumed bijective relationship between a fault's full transient and its position, they can be referred to as transient-based methods (TBM). They have been shown to potentially have a better spatial resolution than standard TWM, relaxing the need for fast-sampling devices. Still, it is not clear what mechanisms enable their higher spatial resolution and how it can be predicted. Moreover, it is not clear how the sampling rate with which the transient is recorded affects the spatial resolution.

This paper attempts to bridge this gap by presenting a theoretical analysis of TBM, first for single lines in Sec. II, where spatial resolution is explained in terms of the resonant frequencies of the line and their sensitivity to a fault position. Results clearly indicate that the spatial resolution is only limited by the line losses and that TBM present super-resolved fault location in resonant lines. Sec. III extends these results to the case of a junction, proving how adding a lateral branch to the line results most often in a loss of spatial resolution, not because of increases losses from the lateral, but rather because of a loss of sensitivity to the fault position, altered by the lateral's own resonances. Sec. IV extends these conclusions to more complex networks, for up to five junctions. Evidence of a similar cause of loss of spatial resolution is presented in Sec. V, where electromagnetic coupling between the conductors in a three-phase line is shown to alter the sensitivity of its resonances to a phase-to-ground fault.

The results presents in this paper have practical implications for the design of accurate fault location methods, providing quantitative tools for estimating how losses and the presence of coupled resonant structures (e.g., laterals) affect their spatial resolution. Understanding the mechanisms behind super resolution should result in a more confident prediction of the accuracy of TBM, and an alternative to the drive towards faster sampling.

II. Faults along a single-phase line

This section presents a first-principle analysis of the spatial resolution of TBM for a simple line. Its main goal is to explain their high spatial resolution on the basis of parameters such as the tested bandwidth, the line length and losses. A single-phase line will be considered, since it allows to derive closed-form results that clearly identify the relationships existing between line parameters and TBM performance. Moreover, single-phase lines have their own practical importance, not only for low- and medium-voltage distribution systems, but also for high-voltage underground power transmission, which could include three-phase lines based on separate coaxial cables, as well as high-voltage DC transmission lines, e.g., used in offshore wind farms and submarine transmission lines [16, Sec. 5]. All these configurations are based on single or separate lines that present no electromagnetic coupling. This last case will rather be discussed in Sec. V for a three-phase overhead line.

The configuration here studied is depicted in Fig. 1, where a shunt fault of impedance Z_S occurs along a line of characteristic impedance Z_o. Assuming $Z_S \ll Z_o$, this configuration may represent the case of a single line as well that of a network, with the fault effectively severing the network into two independent structures, with the probed line terminated by the fault. The analysis is based on forward and backward propagating signals, as defined in transmission-line theory [17, sec. 3.4].

A. Resonance, coherence and spatial resolution

A uniform transmission line of length L is here considered, schematically represented in Fig. 1, terminated by two loads with reflection coefficients Γ_T and Γ_S, e.g., a power transformer and a low-impedance shunt fault, respectively. Both terminations are assumed to be significantly reflective, i.e., with $|\Gamma_S|, |\Gamma_T| \simeq 1$, as discussed in [3]. Sec. II-C will precise the minimum reflectivity required for TBM to have high spatial resolution.

The occurrence of a shunt fault excites a travelling voltage wave $v_f(t)$, the fault surge signal, which will propagate away from the fault and interact with the probe over the transformer, recording the transient voltage $v_m(t)$, after having eventually travelled multiple times across the line.

Defining $v_m^+(t)$ the voltage wave impinging on the probe, transmission-line theory requires that under steady-state conditions the Laplace spectra of these signals must satisfy

$$V_m^+(s) = V_m^+(s)\Gamma_T\Gamma_S \mathrm{e}^{-2\alpha L}\mathrm{e}^{-sT} + V_f(s)\mathrm{e}^{-\alpha L}\mathrm{e}^{-sT/2}, \quad (2)$$

where $s = \mathrm{j}\omega$ is Laplace variable, ω the angular frequency, with v the propagation speed and α the line attenuation constant; $T = 2L/v$ is the round-trip time delay along the line. Recalling that the total voltage at the probe is $V_m(s) = V_m^+(s)(1+\Gamma_T)$, it follows that

$$V_m(s) = V_f(s)(1+\Gamma_T)\mathrm{e}^{-\alpha L}\mathrm{e}^{-sT/2}H(s;L), \quad (3)$$

where the resonant response of the line

$$H(s;L) = \left(1 - \Gamma_T\Gamma_S\mathrm{e}^{-2\alpha L}\mathrm{e}^{-sT}\right)^{-1}, \quad (4)$$

defines the characteristic features of $V_m(s)$; the remaining terms in (3) can be neglected, since they have no impact on either the line characteristic frequencies, or the computation of correlation functions. $H(s;L)$ can be expanded into an infinite sum of simple fractions by applying the residue method

$$H(s;L) = \sum_{m\in\mathbb{Z}\setminus 0} \frac{r_m}{s - p_m}, \quad (5)$$

where $p_m = -1/\tau + \mathrm{j}\omega_m$ are the poles of $H(s;L)$, with

$$\tau = -T/(\ln(|\Gamma_S\Gamma_T|) - 2\alpha L) \quad (6a)$$

$$\omega_m = (2m\pi + \varphi_S + \varphi_T)/T, \quad (6b)$$

while $p_{-m} = p_m$ are their conjugate poles; $r_m = 1/T$ are their respective residues; φ_S and φ_T are the phase-shift angles of the reflection coefficients Γ_S and Γ_T, respectively. For the sake of simplicity, τ will be assumed to be independent of the frequency. It is convenient to introduce the loss factor

$$\delta\Gamma = -\ln(|\Gamma_S\Gamma_T|) + 2\alpha L \simeq 1 - |\Gamma_S\Gamma_T| + 2\alpha L, \quad (7)$$

which will be shown to have a fundamental role in the spatial resolution of TBM.

Grouping pairs of conjugate poles yields

$$H(s;L) = \frac{2}{T}\sum_{m=1}^{\infty}\frac{s+1/\tau}{(s+1/\tau)^2+\omega_m^2} = \frac{2}{T}\sum_{m=1}^{\infty}\psi(s;\tau,\omega_m), \tag{8}$$

i.e., an infinite set of resonances, each described by a Lorentzian function $\psi(s)$.

As recalled in Sec. I, the transient signal measured at the probe and the one estimated for a guessed fault position $\hat{L}$ are compared by means of the correlation (1). Transposed in the frequency domain, this results in

$$\rho(\hat{L}) = \Big(A_m(L)A_m(\hat{L})\Big)^{-1}\int \mathrm{d}\omega\,|V_f(\omega)|^2 H^*(\omega;L)H(\omega;\hat{L}). \tag{9}$$

According to (6) the distance L between the fault and the probe directly affects the frequencies at which the line resonates, as well as their decay time. Hence, any difference between L and $\hat{L}$ would result in a mismatch between the set of resonances, and therefore a loss of correlation between the two transfer functions, indicating that $\hat{L} \neq L$.

The resolution power enabled by a single resonance at ω_m can therefore be quantified by evaluating how fast the correlation (9) decays away from the actual fault position. This can be done in two steps, by first computing the correlation function $\mu(\omega_m, \hat{\omega}_m)$ between the responses of the mth resonance at ω_m of the actual fault position L and that at $\hat{\omega}_m$ for the tested fault distance $\hat{L}$,

$$\mu(\omega_m,\hat{\omega}_m) = \int \mathrm{d}t\ \psi(t;\omega_m)\psi(t;\hat{\omega}_m)\Big/A_\psi(\omega_m)A_\psi(\hat{\omega}_m), \tag{10}$$

where $\psi(t;\omega_m) = \mathrm{e}^{-t/\tau}\cos(\omega_m t)$ is the time-domain response of a single resonance, whose L_2 norm $A_\psi(\omega_m)$ has

$$A_\psi^2(\omega_m) = \frac{\tau}{4}\frac{(\tau\omega_m)^2}{(\tau\omega_m)^2+1} \simeq \frac{\tau}{4}. \tag{11}$$

For reflective loads, the lines can be expected to be resonating, with

$$\omega_m, \hat{\omega}_m \gg 1/\tau \tag{12}$$

for which (10) can be solved and simplifies into

$$\mu(\Delta\omega) = \frac{1}{1+(\Delta\omega\,\tau/2)^2} \tag{13}$$

with $\Delta\omega = \omega_m - \hat{\omega}_m$ the mismatch between the resonance angular frequencies for actual and tested fault positions. The minimum mismatch $\Delta\omega \geq 2\pi B_c$ for which $\mu(\Delta\omega)$ decays by at least 50 % is thus found for

$$B_c = \frac{1}{\pi\tau} = \frac{v\delta\Gamma}{2\pi L}, \tag{14}$$

which represents the coherence or resolution bandwidth of the resonance response. The minimum frequency mismatch B_c can be converted into a spatial resolution by measuring the sensitivity $S(\omega_m)$ with which an error in testing fault positions $\hat{L}$ close to L would shift the resonance frequency $\hat{f}_m = \hat{\omega}_m/2\pi$. From (6b),

$$S(\omega_m) = \frac{\mathrm{d}f_m}{\mathrm{d}L} = -\frac{f_m}{L}, \tag{15}$$

thus a resonance mismatch $\Delta\omega \simeq 2\pi S(\omega_m)\Delta L$. The minimum mismatch distance D_c such that (13) falls off below 50 % is therefore

$$D_c(\omega_m) = \frac{B_c}{|S(\omega_m)|} = \frac{\delta\Gamma}{2\pi f_m/v} = \lambda_m\frac{\delta\Gamma}{2\pi} \tag{16}$$

representing the spatial resolution afforded by each individual resonance in TBM. It is worth noticing that the idea of defining of the spatial resolution based on a resonance sensitivity to fault position and its frequency resolution can be applied to any power-distribution system, even when only numerical or experimental results are available.

The loss factor $\delta\Gamma$, defined in (7), models the impact on the spatial resolution of both propagation and termination losses, which have indistinguishable effects. Therefore, only termination losses will be explicitly discussed in the rest of the paper, in order to reduce the number of parameters involved, with no loss of generality in our conclusions. The spatial resolution in (16) would depend on the fault distance L only for significant propagation losses, compared to losses in the line terminations, as discussed in [18]. This paper will not explore this case, since it focuses on the spatial resolution of TBM, thus close to the actual fault position.

B. Multi-resonance correlation

When the correlation (9) involves data spanning more than one resonance, the resolution (16) no longer holds. It is of practical interest to understand whether in this case the spatial resolution improves with respect to using narrower bandwidths.

The fault surge energy spectrum $|V_f|^2$ will be neglected in the following, assuming either a bandwidth narrow enough for it to be approximatively flat, or equalization signal processing applied to $v_m(t)$, as suggested in [10]. Under these conditions, the numerator of (9) is proportional to

$$\int \mathrm{d}\omega H^\star(\omega;L)H(\omega;\hat{L}) = \frac{4}{T^2}\sum_{p,q=m_1}^{m_2}\int \mathrm{d}\omega\psi^\star(\omega;\omega_p)\psi(\omega;\hat{\omega}_q) \tag{17}$$

i.e., the projection between the resonant responses $H(\omega)$ of the line, included resonances of order $[m_1, m_2]$.

Adjacent resonances are spaced by a distance $\omega_{m+1}-\omega_m = 2\pi/T$, thus the fraction of this spacing occupied by the peak of the Lorentzian responses is of the order

$$2\pi B_c/(\omega_{m+1}-\omega_m) = \delta\Gamma/\pi \ll 1 \tag{18}$$

for a resonant line, hence resonances of different order have a negligible projection. It is therefore possible to approximate (17) by only looking at the projections between same-order resonances, yielding a correlation

$$\begin{aligned}\rho(\Delta L) &= N^{-1}\sum_{p=m_1}^{m_2}\mu(2\pi S(\omega_p)\Delta L)\\ &= N^{-1}\sum_{p=m_1}^{m_2}\frac{1}{1+(\Delta L/D_c(\omega_p))^2}\end{aligned} \tag{19}$$

with the single-resonance correlation $\mu(\Delta\omega)$ given in (13) and $N = m_2 - m_1 + 1$ the number of resonances occurring within

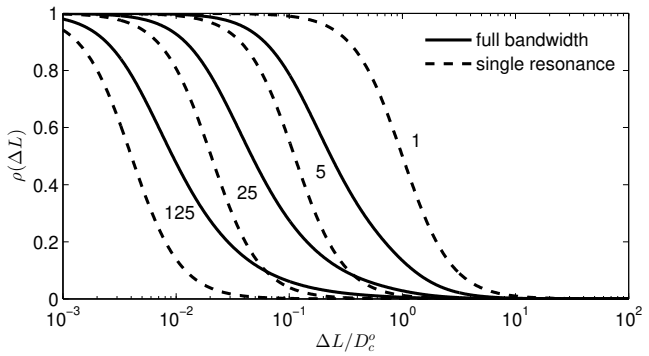

Fig. 2. Expected spatial resolution $\rho(\Delta L)$ when testing fault positions from data covering all resonances of order $p \in [1, m_2]$, with $m_2 = 1, 5, 25$ or 125 (solid lines) predicted by (20), and for a single resonance $p = m_2$ (dashed lines) predicted by (13). The distance from the fault, ΔL, is normalized to the spatial resolution expected for the first resonance, with order $p = 1$.

the tested bandwidth. The L_2 norm A_H is directly found from (11), assuming equal decay times τ for the N resonances, with $A_H^2 \simeq N\tau^2/4$.

From (6b), for the case of practical interest where $\varphi_T = 0$ and $\varphi_S = \pi$[1], the p-th order resonance has $\omega_p = (2p-1)\omega_1$, thus from (16) and (19)

$$\rho(\Delta L) = N^{-1} \sum_{p=m_1}^{m_2} \frac{1}{1 + (\Delta L/D_c^o)^2 (2p-1)^2} \tag{20}$$

with $D_c^o = D_c(\omega_1)$ the spatial resolution associated to the first resonance of the line. Fig. 2 shows $\rho(\Delta L)$ for $m_1 = 1$ and $m_2 = 1, 5, 25, 125$, where the condition $\rho(\Delta L) = 1/2$ is reached for distances about 2.1 times larger than the corresponding D_c expected for a single resonance at the high-frequency end, i.e., for $p = m_2$. This systematic and significant loss of spatial resolution is fundamentally due to the lower resolution associated to low-frequency resonances, and explains why including low-frequency data in the computation of the correlation is not necessarily an optimal choice.

The rest of the paper shows that this issue is more general, with resonances that can abruptly loose resolution and potentially limit the fault location accuracy if included in the computation of the correlation.

C. Super-resolved fault location

The spatial resolution of each resonance is predicted by (16) to potentially be a fraction of the wavelength λ_m, depending on the value of the loss factor $\delta\Gamma$. The spatial resolution is enabled by the resonant behavior of the line, and its inherent sensitivity to a change in fault distance makes TBM, at the scale of a single resonance, work in a way similar to Fabry-Pérot interferometers, converting a change in length into a change in the resonance frequency. This principle is rather used the other way around in fault location, where the spatial resolution is limited by the minimum change in tested fault positions for which the resonant response $H(\omega)$ changes significantly.

[1]i.e., for a high-impedance transformer at the probe end and a low-impedance shunt fault, respectively.

Standard TWM and, equivalently, time-domain reflectometry methods, are subject to more fundamental limitations in their spatial resolution, due to the Fourier transform uncertainty principle [19, Sec. 3], which states that for a signal whose spectrum has a standard deviation σ_f, its time-domain standard deviation σ_t is bounded to be

$$\sigma_t \geq 1/4\pi\sigma_f, \tag{21}$$

implying that its time resolution can be improved only by increasing its frequency bandwidth. Taking the case of a signal with a flat spectrum over a bandwidth $[0, f_m]$, which is proportional to $\mathrm{sinc}(2\pi f_m t)$, its time support can be measured by the time Δt required to see its amplitude reduced by a factor 50 % from its peak value, i.e.,

$$\Delta t = \frac{1.89}{2\pi f_m}, \tag{22}$$

which corresponds to a spatial resolution $\Delta x = v\Delta t$, with v the propagation speed along the line under test. Comparing it with (16) finds

$$\frac{D_c}{\Delta x} = \frac{\delta\Gamma}{1.89} \tag{23}$$

which is significantly smaller than one for a resonant system, for which $\delta\Gamma \lesssim 1$. Hence, a single resonance using TBM can afford a better spatial resolution than with pulse-based methods, such as time-domain reflectometry. Notice how the fault surge signals used in TWMs do not have flat spectra, and should therefore be expected to display a significantly lower spatial resolution than (22).

The possibility of having $D_c < \Delta x$ is referred to in imaging-method literature as super resolution, since it bypasses the resolution limitation (21). This property was demonstrated using results derived under two main assumptions: a) significant resonances, as required by (12), i.e.,

$$B_c/f_m \ll 2 \tag{24}$$

and b) separate resonances, which under (18) requires

$$\delta\Gamma \ll \pi, \tag{25}$$

which is the most stringent. Both are verified as soon as $\delta\Gamma \lesssim 1$, i.e., significantly smaller than one, but not necessarily negligible. Considering only termination losses in an impedance Z, this condition requires that $Z/Z_o \lesssim 1/2$, or $Z/Z_o \gtrsim 2$. Moreover, (7) implies that $\delta\Gamma \lesssim 1$ only if propagation losses are low enough, with $2\alpha L \lesssim 1$. Given that propagation losses significantly increase with the frequency, TBM can present super resolution most likely below the MHz range. Results of TBM applied to lossy lines are found in the EMTR literature [11], [12] and in [18], where the reported location accuracy is consistent with the super-resolution property.

D. Simulation results

Numerical simulations were run using EMTP-RV, for a single-phase lossless overhead line consisting of a conductor 10 mm in diameter, 7.5 m above a lossless ground, corresponding to per-unit-length parameters $L = 1.6$ mH/km and $C = 6.95$ nF/km and a characteristic impedance $Z_c = 480\,\Omega$.

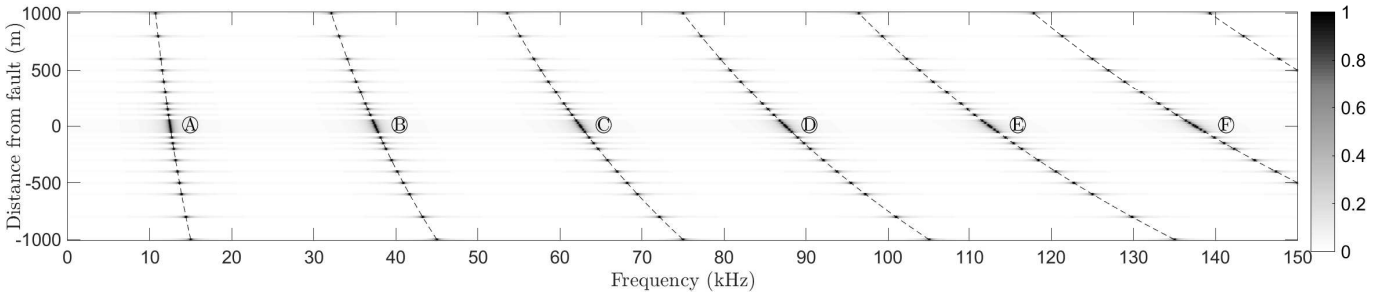

Fig. 3. Resonant response $H(\omega, \hat{L})$ between the fault and the probe for a line of length $L = 6$ km, as a function of frequency and the distance between the tested and actual fault positions, $\hat{L} - L$. Dashed lines track the resonance frequency predicted by (6b).

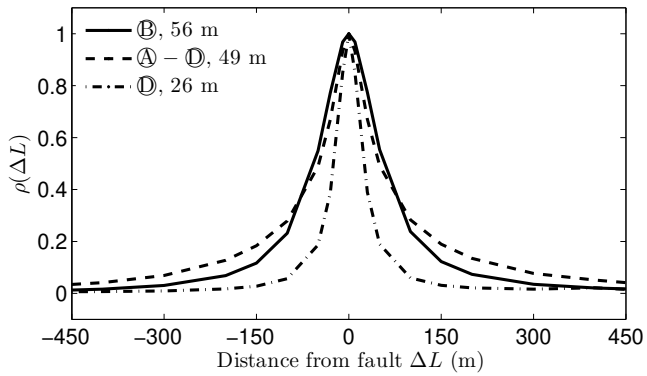

Fig. 4. Correlation functions for the transfer functions in a line with a fault 6 km from the probe, for three choices of test bandwidths, covering either a single or multiple resonances, shown in Fig. 3. The spatial resolution of each configuration is reported in the legend.

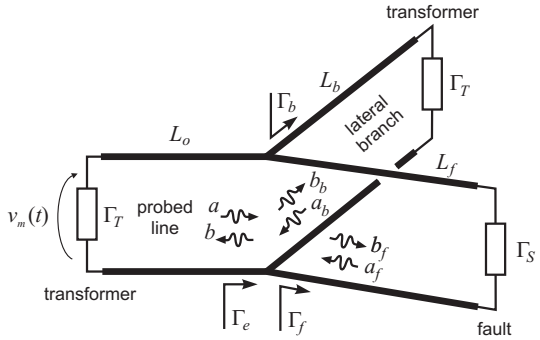

Fig. 5. Equivalent description of a single-phase network where the fault occurs after a junction with a lateral branch.

The fault impedance was set to $Z_S = 10\ \Omega$ [20] and the transformer termination to $Z_T = 100$ kΩ [3], [21] corresponding to reflectivities $\Gamma_S = -0.96$ and $\Gamma_T = 0.99$. All parameters are considered to be frequency independent for the sake of simplicity.

The transfer function between the fault surge $V_f(\omega)$ and the measured voltage $V_m(\omega)$ at the line terminal were computed for a fault 6 km away from the probe. Test positions around the actual fault were also considered, spanning $|\Delta L| \leq 1$ km on both sides. The results were obtained for frequencies up to 1 MHz, in 10 Hz steps. Fig. 3 shows how resonances shift when testing different fault positions $\hat{L}$. Their spatial resolutions D_c where estimated as explained in the Appendix and found to be accurate to within $\pm 1\%$ of the values predicted by (16).

The correlation between the transfer function for the actual fault position and those at each tested position $\hat{L}$ were computed for three different bandwidths, in order to verify the effect of using data covering a varying number of resonances. A continuous bandwidth from 10 to 105 kHz, covering four resonances from Ⓐ to Ⓓ (cf. Fig. 3) is used as a reference against which single-frequency results at compared: a) for resonance Ⓑ at 37.4 kHz, testing the bandwidth 25-50 kHz and resonance Ⓓ at 87.3 kHz, over the bandwidth 75-105 kHz. The results shown in Fig. 4 support the conclusions given in Sec. II-B, with resonance Ⓓ presenting a resolution of 26 m, about half of the one obtained including low-frequency data, for 10-105 kHz, equal to 56 m, in agreement with the prediction of a resolution loss by a factor 2.1 predicted in Sec. II-B. Resonance Ⓑ offers practically the same resolution with 49 m, while requiring data acquired at half the maximum frequency.

III. Impact of a lateral branch

The previous section has shown how the spatial resolution can be predicted by tracking the sensitivity and coherence bandwidth of each system resonance. That analysis is here extended to the configuration in Fig. 5, where fault transient signals have to cross a junction with a lateral branch before reaching the probe.

The introduction of a lateral could be expected to introduce a significant increase in losses, with the transient now interacting with the termination impedance of the lateral branch and being attenuated along it. Higher losses could then be expected to result in a loss of spatial resolution of TBMs. The results shown in this section disprove this interpretation, since a lateral branch does not necessarily lead to higher losses. A potential loss of spatial resolution is indeed demonstrated, even in case of very weak losses, but is rather explained by a counterintuitive loss of sensitivity of the system resonances to a change in the tested fault position.

In spite of the apparent simplicity of this network, the introduction of a single lateral branch will be shown to introduce a high degree of variability in the sensitivity and frequency resolution of the resonances observed along the

probed line, phenomena predicted and explained by the proposed theoretical derivation.

From the viewpoint of the probe monitoring a power network, the only difference between the structures in Figs. 1 and 5 is that the fault, with reflectivity Γ_S, along the probed line is now substituted by an equivalent reflection coefficient Γ_e, representing the rest of the network at the right of the junction. The probed line has a length L_o and the fault is found at a total distance $L_o + L_f$ from the probe. The lateral branch, of length L_b, is terminated by the same load Z_T found at the probed end, modeling a transformer.

A. Equivalent termination and effective lengths

The equivalent reflection coefficient $\Gamma_e(\omega)$ can be derived by establishing a set of equations involving the forward and backward voltage waves along each branch of the junction, as defined in Fig. 5

$$\begin{aligned} a_f &= \Gamma_f b_f = \Gamma_S \mathrm{e}^{\mathrm{j}\varphi_f} b_f \\ a_b &= \Gamma_b b_b = \Gamma_T \mathrm{e}^{\mathrm{j}\varphi_b} b_b \\ (b, b_f, b_b)^T &= \mathbf{S}_J (a, a_f, a_b)^T \end{aligned} \tag{26}$$

where $\mathbf{S}_J = 2/3 - \mathbf{1}$, is the scattering matrix of a three-way junction [17, Sec. 4.7], with $\mathbf{1}$ the identity matrix and

$$\begin{aligned} \varphi_f &= -2\beta L_f \\ \varphi_b &= -2\beta L_b \end{aligned} \tag{27}$$

the round-trip propagation phase shifts along the fault and lateral branches, respectively, with $\beta = \omega/v$ the propagation constant. Propagation losses along each branch would reduce the reflection coefficients of their respective terminations, requiring to substitute $\Gamma_S \rightsquigarrow \Gamma_S \exp(-2\alpha L_f)$ for the branch where the fault occurs, and similarly for the lateral. In the following, because they are fundamentally equivalent to using a different reflection coefficient, we do not explicitly discuss propagation losses, in order to limit the number of parameters in the analysis, with no loss of generality.

The equivalent reflection coefficient is obtained as $\Gamma_e(\omega) = b(\omega)/a(\omega)$ by solving (26), yielding

$$\Gamma_e(\omega) = \frac{-1 + \Gamma_b(\omega) + \Gamma_f(\omega) + 3\Gamma_b(\omega)\Gamma_f(\omega)}{3 + \Gamma_b(\omega) + \Gamma_f(\omega) - \Gamma_b(\omega)\Gamma_f(\omega)}. \tag{28}$$

From (28) it is possible to straightforwardly verify how much change in the loss factor should be expected by adding a lateral. For the case of two branches with low input impedance, e.g., with $\Gamma_f = \Gamma_b = -0.9$, the reflectivity seen from the junction would actually increase to $\Gamma_e = -0.95$, while for two high-impedance branches, e.g., with reflectivities equal to 0.9, then $\Gamma_e = 0.81$, i.e., a lower reflectivity. The loss factor would thus pass from 0.1 to 0.05 for the first case, while the second would see it pass from 0.1 to 0.19. In both cases the conditions required for super-resolved fault location in Sec. II-C would still hold and would not lead to expect a significant loss in the spatial resolution. This section will prove that a lateral branch may result in a loss of spatial resolution not because of higher losses, but rather because of a reduction in the sensitivity of the system resonances to a change in the tested fault position.

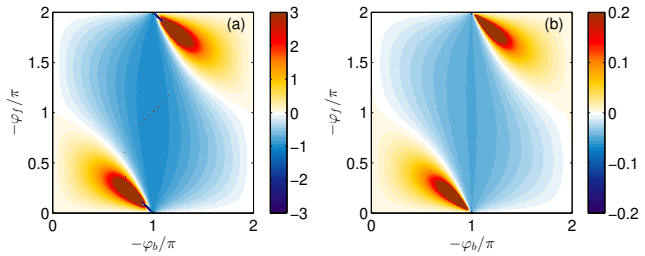

Fig. 6. Equivalent reflection coefficient Γ_e for a junction between two laterals, terminated by loads of reflectivity $\Gamma_T = 0.99$ (transformer) and $\Gamma_S = -0.96$ (shunt fault). (a) phase perturbation $\delta = \partial\delta\varphi_e/\partial\varphi_f$, introduced in (30) to explain change in the resonance sensitivity; (b) additional loss term $\ln|\Gamma_S/\Gamma_e|$, introduced in (34). The dark red regions in (b) indicate higher losses, with $|\Gamma_e| \ll |\Gamma_S|$, consistently with (35).

The resonance frequencies of the probed line are still described by (6b), by replacing the fault coefficient Γ_S with Γ_e. It is convenient to expand the phase-shift angle φ_e of Γ_e as $\varphi_e = \varphi_f + \varphi_S + \delta\varphi_e$, in order to identify the apparent change in phase-shift angle $\delta\varphi_e$ properly due to the junction, as opposed to the phase-shift angle expected in case no lateral branch were present.

The definition of resonance sensitivity (15) can be applied to the present case, with respect to the fault distance L_f,

$$S'(\omega_m) = \frac{\mathrm{d}f_m}{\mathrm{d}L_f} = -\frac{f_m}{L_e}, \tag{29}$$

leading to the definition of the effective distance $L_e(\omega)$ by analogy with (15). From (6b) and (29)

$$L_e(\omega) = (L_o + L_f)\left(1 + \frac{\partial\delta\varphi_e}{\partial\varphi_f}\right)^{-1}, \tag{30}$$

showing that the term $\partial\delta\varphi_e/\partial\varphi_f$ measures how the lateral branch alters the sensitivity of a resonance to the fault position. Evaluating Γ_e in (28) for $\Gamma_T = 0.99$ and $\Gamma_S = -0.96$ as for the single-line in Sec. II-D, Fig. 6(a) shows how $\partial\delta\varphi_e/\partial\varphi_f$ evolves as a function of the fault and lateral branch phase-shift angles (27), with the large central region of values close to -1 corresponding to an apparent distance $L_e \gg L_o + L_f$, with $L_e \to \infty$ for $\varphi_b \to -\pi$. Fig. 7(a) represents the loss of sensitivity of with respect to the case with no lateral, i.e.,

$$S/S' = L_e/(L_o + L_f). \tag{31}$$

Positive values of $\partial\delta\varphi_e/\partial\varphi_f$ are also observed for two small drop-shaped regions in Fig. 6(a), for which (30) rather predicts an increased sensitivity. Evidence of these two opposite phenomena is presented in Sec. III-B.

Updating the original definition (14) of the coherence bandwidth first requires to acknowledge that the probe-fault distance there appearing represented the propagation delay T in (6a) and the loss factor (7). A distinct apparent distance L'_e is therefore introduced, modeling changes in the apparent propagation delay, rather than the resonance sensitivity. As proven below, $L'_e \neq L_e$ in presence of a lateral branch.

For a fault along a single line at a distance L_f, a propagation phase shift $\varphi_f = -2\beta L_f$ would follow. When a junction is

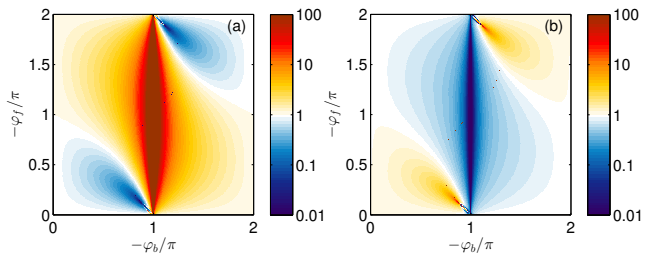

Fig. 7. Impact of a lateral branch with termination reflectivity $\Gamma_T = 0.99$ on the location of a fault with reflectivity $\Gamma_S = -0.96$. (a) sensitivity loss $L_e/(L_o + L_f)$, defined in (31) and (b) spatial resolution gain D_c/D'_c, with respect to the case where no junction is present.

present φ_e replaces φ_f, and a similar expression of the phase shift can be sought, writing $\varphi_e = -2\beta\delta L'_e + \varphi'_e$. Here $\delta L'_e$ is the apparent distance between the junction and the fault, explaining the overall propagation phase shift, while φ'_e is the portion of φ_e not explained by a propagation delay.

The apparent distance $\delta L'_e$ is therefore given by

$$\delta L'_e(\omega) = -\frac{v}{2}\frac{\partial\varphi_e}{\partial\omega} = -\frac{v}{2}\frac{\partial(\varphi_f + \delta\varphi_e)}{\partial\omega} = L_f - \frac{v}{2}\frac{\partial\delta\varphi_e}{\partial\omega}, \tag{32}$$

with an overall apparent distance from the probe

$$L'_e(\omega) = L_o + \delta L'_e = L_o + L_f\left(1 + \frac{\partial\delta\varphi_e}{\partial\varphi_f}\right). \tag{33}$$

The importance of defining two effective lengths can be appreciated for the cases when the lateral branch presents a low input impedance to the junction, potentially shunting the fault line. Fig. 6(a) shows this case for $\varphi_b = -\pi$, with $\partial\delta\varphi_e/\partial\varphi_f \to -1$. In this case, a change in the tested fault position would have little effect on Γ_e, reducing sensitivity of the resonances observed along the probed line, consistent with $L_e \gg L_o + L_f$ predicted by (30). With the lateral shunting the fault branch, transients recorded by the probe would decay with a time constant dictated by L_o, consistent with (33) predicting $L'_e \to L_o$.

The effective loss factor[2] for the probed line terminated by a junction is obtained from (7) by also substituting Γ_S with Γ_e, thus

$$\delta\Gamma' = -\ln(|\Gamma_e\Gamma_T|) + 2\alpha L_o = \delta\Gamma + \ln(|\Gamma_S/\Gamma_e|) - 2\alpha L_f, \tag{34}$$

with $\delta\Gamma$ the dissipation factor expected without the lateral branch, as given in (7).

Eq. (34) predicts an incremental loss $\ln(|\Gamma_S/\Gamma_e|)$. This term is shown in Fig. 6(b), where it appears that the lateral branch is more likely to lead to lower termination losses from the probe viewpoint, indicated by the blue region. This result is explained by the fact that $|\Gamma_T| > |\Gamma_S|$, so that the lateral branch can enforce a higher reflectivity at the junction when it partially shunts the faulty branch. In this case, the frequency resolution of the system resonances, measured by B_c, would appear to be improving.

[2]measuring the *apparent* dissipation of the system as seen from the probe

The opposite phenomenon occurs in the red regions, where the equivalent reflectivity at the junction becomes lower than that of the fault branch, indicating higher losses. This behavior is maximal in the dark red regions, with a significantly lower reflectivity at the junction that could be interpreted as an increase in power dissipation, even with both branches terminated by reflective loads. This outcome, which Fig. 6(b) shows to have low probability, is not explained by a potential joint dissipation from both lateral and fault branches, but is rather the result of destructive interference from reflected waves a_b and a_f, as defined in Fig. 5.

Indeed, (28) even admits $|\Gamma_e| = 0$, i.e., a perfectly matched probed line at the junction end, corresponding to an apparent total dissipation, for

$$\Gamma_b = \frac{1 - \Gamma_f}{1 + 3\Gamma_f}, \tag{35}$$

corresponding to a single point within the dark red regions of Fig. 6(b). The possibility of observing $|\Gamma_e| \simeq 0$ amounts to a risk of missing the presence of the fault at certain frequencies, since the probed line could no longer sustain a resonance in this case. Sec. III-B presents direct evidence of this counterintuitive phenomenon.

From (7), (14), (33) and (34), the coherence bandwidth updates to

$$B'_c(\omega_m) = \frac{v\delta\Gamma'}{2\pi L'_e} = v\frac{-\ln(|\Gamma_e\Gamma_T|) + 2\alpha L_o}{2\pi L'_e}, \tag{36}$$

which, together with (29), leads to a spatial resolution

$$D'_c(\omega_m) = \frac{v\delta\Gamma'}{2\pi L'_e}\frac{L_e}{f_m} = \lambda_m\frac{\delta\Gamma'}{2\pi}\frac{L_o + L_f}{(1+\delta)\left(L_o + L_f(1+\delta)\right)}, \tag{37}$$

where $\delta = \partial\delta\varphi_e/\partial\varphi_f$. This result converges back to (16) as soon as $\delta \to 0$. In any other case, D'_c is no longer independent from the fault position, as was the case in (16) for a single line, as indeed observed in Sec. III-B.

The impact of the lateral branch on the accuracy of fault location is quantified in Fig. 7(b), in terms of the resolution gain D_c/D'_c: a value larger than one would mean that the spatial resolution D'_c, in presence of the lateral branch, is

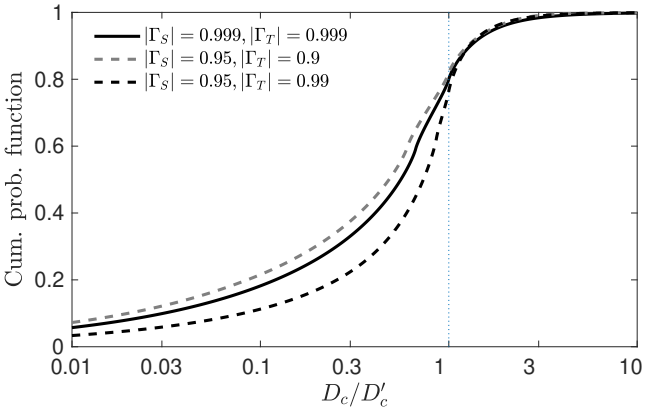

Fig. 8. Cumulative distribution function of the resolution gain D_c/D'_c , obtained for several choices of line termination and fault reflection coefficients.

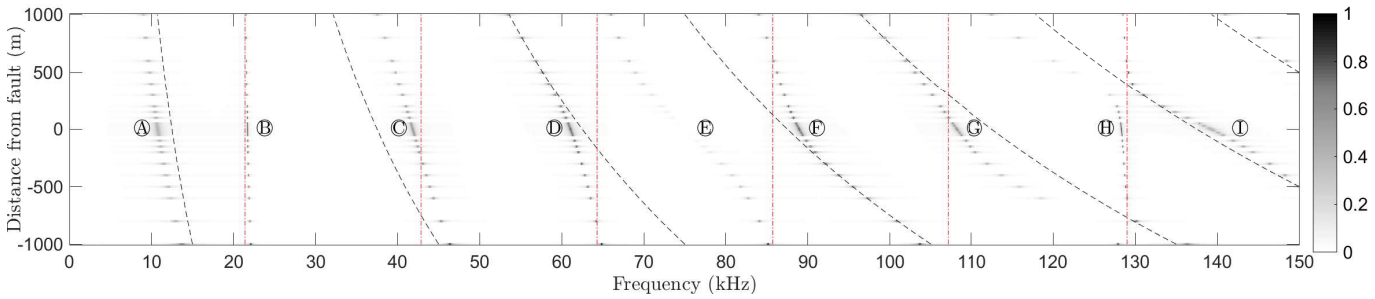

Fig. 9. Resonant response for the single-junction network in Fig. 5, with $L_o = 4$ km, $L_f = 2$ km and $L_b = 3$ km, as a function of frequency and tested fault position. Dashed black lines track the resonance frequencies predicted by (6b) when no lateral branch is present, while red dash-dot lines show those expected when the lateral branch shunts the fault branch, e.g., it has a much lower input impedance.

better (i.e., with a smaller support). In most cases $D'_c > D_c$ (blue region), with the lateral branch degrading the spatial resolution, by reducing the sensitivity of the system resonances (cf. Fig. 7(a)), without a corresponding increase in dissipation (cf. Fig. 6(b)). Yet, Fig. 7(b) also predicts the existence of smaller regions where the junction could have a beneficial impact, improving the spatial resolution (darker red regions).

Fig. 8 summarises these results by means of the cumulative probability distribution (cdf) of the values taken by the resolution gain D_c/D'_c, for several choices of line termination and fault reflectivities. A spatial resolution improved by a factor $D_c/D'_c > 2$ is found only 3 % of the time in all the cases considered, whereas the risk of seeing it degraded by a factor larger than two passes is between 33 % and 51 %, indicating a significant risk of resolution loss with respect to the single-line case.

It can be remarked how a higher probability of resolution loss is not systematically observed for more dissipative terminations, with very similar results obtained for a very weakly dissipative configuration ($|\Gamma_S| = 0.999, |\Gamma_T| = 0.999$) and a significantly more dissipative one ($|\Gamma_S| = 0.95, |\Gamma_T| = 0.9$). These results support the thesis that resolution is mostly lost due to a reduction in the sensitivity of the resonances caused by the lateral branch.

Coherently with these observations, the effective distance L_e can be shown to be a good estimator of the spatial resolution loss, as soon as $L_e \gg L_o + L_f$, i.e., when the lateral is partially shunting the fault branch. In this case, $|\Gamma_e| \simeq |\Gamma_T|$, for which (36) converges to

$$B_c^{\infty} = \frac{v\delta\Gamma''}{2\pi L_o} \tag{38}$$

with $\delta\Gamma'' = -\ln(|\Gamma_T|^2) + 2\alpha L_o$. Hence, (37) simplifies into

$$D_c^{\infty} \simeq \lambda_m \frac{\delta\Gamma''}{2\pi} \frac{L_e}{L_o}. \tag{39}$$

Therefore, resonances sharing the same L_e present a spatial resolution improving with the frequency, as found for a single line in (16), but worsening for higher values of L_e. Hence, estimating L_e from the sensitivity of a resonance to the fault position would help to identify resonances with poor spatial resolution that might better be filtered out when processing fault transient spectra.

B. Numerical results

EMTP-RV numerical simulations were run for the network in Fig. 5, for $L_o = 4$ km, $L_f = 2$ km and $L_b = 3$ km, for a maximum frequency of 1 MHz, with the same line parameters used in Sec. II-D for a single line, using terminations with reflectivities $\Gamma_S = -0.96$ for the shunt fault and $\Gamma_T = 0.99$ for the transformers. The fault is found at the same distance from the probe in both cases, with the only difference being the introduction of the lateral branch. The main advantage of this choice of analysis is that any change in the behavior of the system and the fault location accuracy can be traced back to the introduction of the lateral. As discussed in Sec. III-A, propagation losses can be considered by simply reducing the modulus of the reflection coefficients Γ_S and Γ_T chosen for the terminations of the faulty and lateral branches, with no approximation in the results.

Fig. 9 tracks the resonances of the transfer functions between fault and probe, for tested fault positions close to the actual one. Theoretical results for the case without lateral branch, first shown in Fig. 3, are reported for comparison (black dashed lines), highlighting the perturbation introduced by the lateral branch. When the system resonances occur close to those of the lateral (red dashed lines), they are hardly sensitive to the fault position, e.g., Ⓑ and Ⓗ, indicating that the lateral is partially shunting the fault branch. The resonance Ⓔ can be seen to practically vanish at the fault position, corresponding to the destructive-interference condition (35).

The effective length L_e and frequency resolutionB'_c of each resonance for the actual fault position were estimated as described in the Appendix. Fig. 10 shows their wide range of variation and their apparent random behavior. The effective length L_e, measuring the sensitivity of each resonance to change in the tested fault position, appears to be potentially much larger than the actual probe-fault distance. The frequency resolution B'_c is shown to mostly swing between B_c^{∞} and B_c. These two values correspond to the extreme cases where either the lateral branch or the faulty branch control the equivalent termination impedance at the junction, with one of them presenting a significantly lower impedance than the other. Higher losses are also found in Fig. 10, e.g., for the first resonance, with a larger B'_c. This configuration corresponds to the light red regions in Fig. 6(b).

Fig. 10 also reports theoretical results predicted by (30),

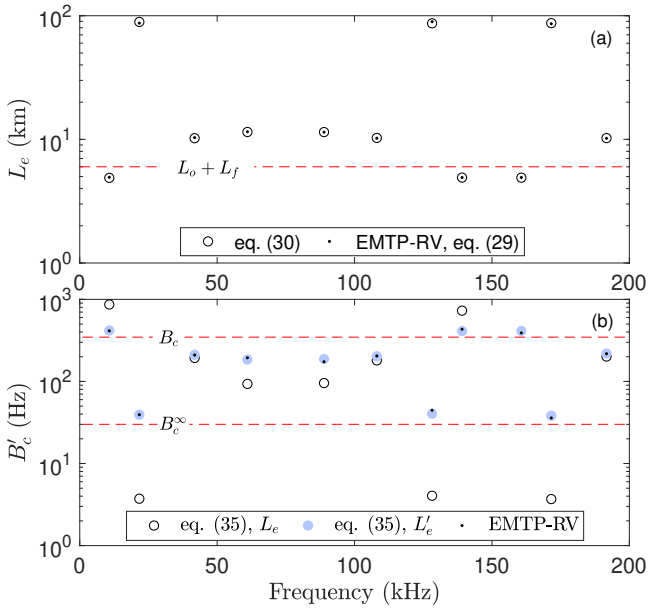

Fig. 10. Effective fault distance L_e (a) and coherence bandwidth B_c' (b) for the single-junction network in Fig. 5, estimated from the models introduced in Sec. III-A based on two distinct effective lengths, here validated by results estimated from EMTP-RV simulations, as explained in the Appendix.

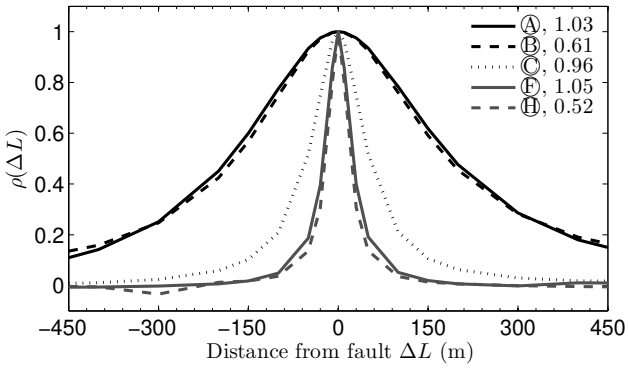

Fig. 11. Correlation functions for the transfer functions of the single-junction network in Fig. 5, obtained from EMTP-RV results covering only a single resonance at the time (cf. 9). The resolution gain D_c/D_c' predicted for each resonance is shown in the legend.

(33) and (36), confirming the accuracy of the model proposed in Sec. III-A to explain the impact of a lateral branch. The importance of defining two distinct effective lengths is thus confirmed: using L_e instead of L_e' to estimate B_c' would lead to significant errors. Furthermore, the pivotal role of $\partial\delta\varphi_e/\partial\varphi_f$ is confirmed, explaining the change in the both sensitivity to fault location and frequency resolution of the resonances.

The practical impact of the changes in the behavior of the system resonances can be better appreciated in Fig. 11, which shows the correlation (9) between the transfer functions for the actual and tested fault positions, computed over bandwidths covering a single resonance at the time, in order to highlight differences in their individual spatial resolutions. The gain in spatial resolution D_c/D_c' of each resonance, defined with respect to the single-line theory, is also reported there.

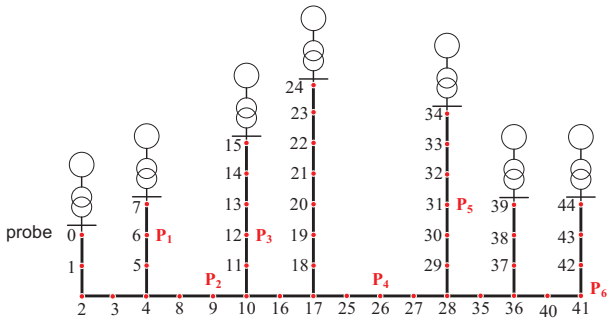

Fig. 12. The five-junction network considered in Sec. IV, based on single-phase lines. Each node is at a distance of 1 km and the nominal fault positions are tagged P_1 to P_6. The probe is marked by the tag 0. Each lateral branch is terminated by a load with reflectivity $\Gamma_T = 0.99$, while the fault has a reflectivity $\Gamma_S = -0.96$.

Resonances Ⓐ and Ⓑ have practically identical correlation functions, although Ⓑ's occurring at a higher frequency would be expected to afford a higher resolution: a resolution gain about 0.61 is found instead. A similar phenomenon is observed for resonance Ⓗ. Marginal resolution improvements, smaller than 5 %, are also reported for Ⓐ and Ⓕ. These results confirm the significant and seemingly random loss of resolution power that can be experienced in case a junction is present.

IV. Spatial Resolution in Networks

Since Sec. III takes as vantage point the probe, it can be readily applied to more complex networks. While closed-form results of L_e and L_e' as functions of the fault distance are no longer valid, the general behavior of spatial resolution in presence of a complex network can be expected to undergo the same phenomena pointed out in Sec. III-B, in particular the significant risk of resolution loss, caused by a loss of sensitivity of the system resonances to the tested fault positions, rather than increased losses from added lateral branches.

In order to prove this point, the five-junction network in Fig. 12 was simulated using EMTP-RV, from DC up to 1 MHz, considering the same line parameters used with the single-line and single-junction configurations, using terminations with reflectivities $\Gamma_S = -0.96$ for the shunt fault and $\Gamma_T = 0.99$ for the transformers at the end of each lateral branch. The probe is at the end of a line, marked by the tag 0 and six fault positions were considered, marked as P_1 to P_6, distributed at a distance ranging from 6 to 17 km from the probe. The rationale being to understand whether an increasing number of junctions between probe and fault leads to major differences with respect to the case of a single junction. Given that the shunt fault would practically severe the network into two parts, depending on the fault position only a few junctions will affect the transient, e.g., a fault in P_1 would see five junctions interacting with the fault transient, while a fault in P_4 would have only three. As in previous simulations, for each fault position, other tested positions were simulated around each fault, constituting the dictionary used by correlation methods (and in general by TBM) to locate a fault.

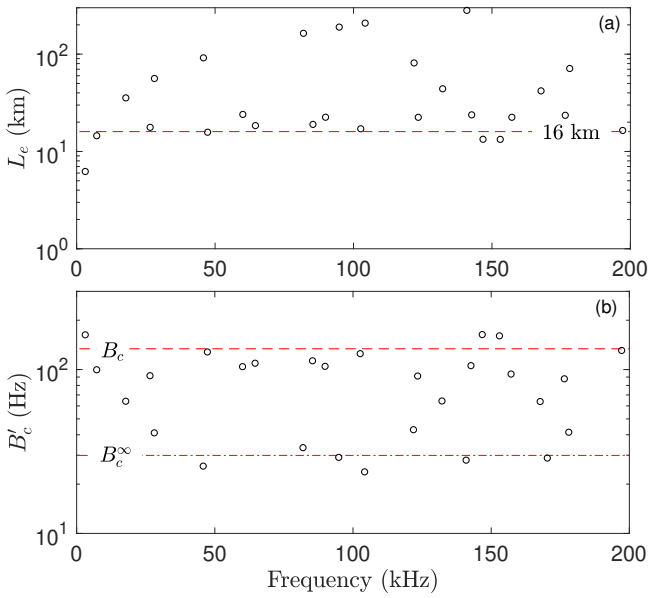

Fig. 13. Effective fault distance L_e (a) and coherence bandwidth B'_c (b) for a fault at position P_5 in the network in Fig. 12. Results estimated from EMTP-RV simulations, as explained in the Appendix.

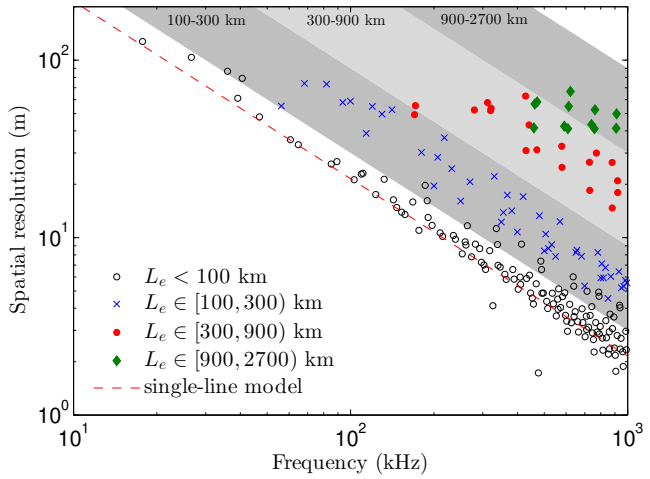

Fig. 14. Spatial resolution D'_c of each resonance obtained from EMTP-RV results for a fault at the position P_5 for the configuration in Fig. 12, as a function of frequency. Data are sorted according to their effective length L_e. Theoretical results (red dashed line) were computed for a single-line 16 km long, i.e., with no lateral branches.

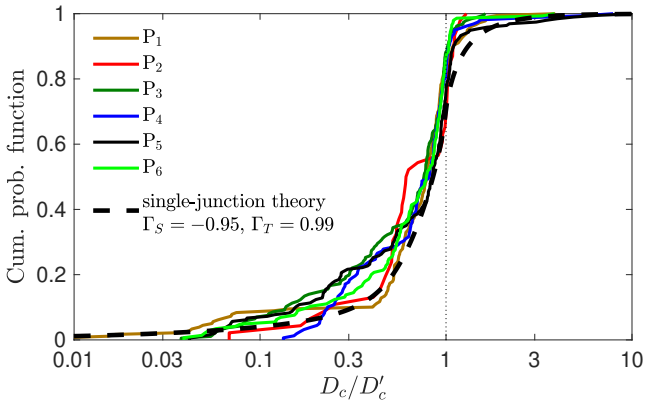

Fig. 15. Empirical cdf distribution of the resolution gain D_c/D'_c for the network in Fig. 12, computed from EMTP-RV simulations, for six fault positions, P_1 to P_6. The dashed line is the theoretical cdf shown in Fig. 8 for a single-junction network, for the same choice of Γ_S and Γ_T.

The effective length L_e and frequency resolution B'_c were estimated from the simulation results, as described in the Appendix. Fig. 13 shows results obtained for a fault at the position P_5, confirming that even with five junctions involved, the frequency resolution is not systematically degraded, as would be expected for increased dissipation along the larger number of branches. Rather, the range of variation of B'_c closely agree with that observed and predicted in Sec. III for a single junction. Cases of higher apparent losses are observed just for a minority of the resonances, with B'_c attaining 160 Hz, instead of the 133 Hz predicted if no junction were present. Also similar to the case of a single junction, the sensitivity of the system resonance can be strongly reduced, as witnessed by the large values of L_e, often exceeding hundreds of km.

These results were further processed, in order to test the validity of the asymptotic model (39), which relates the spatial resolution D'_c of a resonance to its effective length and sensitivity. Fig. 14 presents the results obtained for a fault at P_5. First, it confirms the inverse dependence existing between the spatial resolution D'_c and the frequency of resonance, as predicted by the single-line theory (16), for values of L_e not much larger than the direct fault-probe distance, here equal to 16 km. This agreement implies that at these frequencies lateral branches present a high input impedance at their associated junctions, and therefore have a negligible impact on the spatial resolution. But as soon as $L_e \gg 16$ km, (39) predicts a loss of resolution proportional to L_e, consistent with the numerical results, which are divided into three sets of resonances covering different ranges of values of L_e. The shaded areas in Fig.14 indicate the regions of spatial resolution predicted by (39). These results confirm that a large ratio between the effective length L_e and the direct probe-fault distance would indicate a risk of significant resolution loss. L_e can be estimated from the reference data required by TBM for different test fault positions, without further simulations.

Noting D_c the spatial resolution expected from the single-line theory (16), i.e., neglecting lateral branches, the resolution gain D_c/D'_c was finally computed, in order to assess whether it depends on the number of junctions and laterals. The cdfs of D_c/D'_c obtained for the six fault positions P_1 to P_6 are shown in Fig. 15. These results present very similar features, suggesting that the number of junctions have a minor impact on the variability of the spatial resolution. Interestingly, the first distribution shown in Fig. 8 for the single-line theory, corresponding to the same terminations used in the network in Fig. 12, closely reproduces the main features of the cdfs. These results confirm that the models derived in Sections II and III apply also to complex networks, and that a sizeable fraction of their resonances present a significant loss of resolution. Moreover, these results confirm that the main mechanism

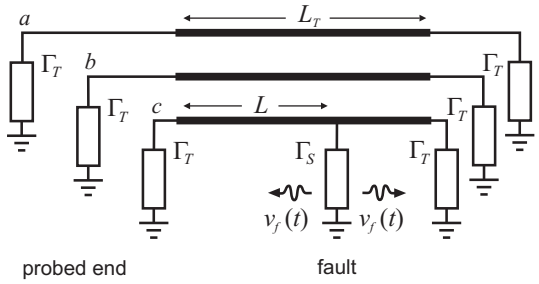

Fig. 16. The three-phase line of length L_T simulated with EMTP-RV, with each phase terminated by identical loads with reflectivity $\Gamma_T = 0.99$, and a phase-to-ground fault of reflectivity $\Gamma_S = -0.96$ at a distance L along phase c. Fault-probe transfer functions were computed for each phase, marked a to c.

behind resolution loss is the reduction of sensitivity to the tested fault position, studied in detail in Sec. III. Hence, the network topology has little impact on the statistical behavior of spatial resolution, which is rather explained by phenomena occurring at the level of a single junction, with negligible cumulative effects.

V. Phase-to-ground fault in a three-phase overhead line

A case of practical importance for power transmission is represented by three-phase overhead lines. Shunt faults can take a number of different configurations, by appearing across phases as well as toward the ground [20], thus making a direct extension of the theory proposed in Sec. II difficult.

This section will focus on the case of a phase-to-ground fault, involving a single phase, as depicted in Fig. 16 , which is the most likely shunt fault configuration [20, Sec. 3]. For this case, the phase along which the fault occurs can be regarded as an extension of the single-line configuration studied in Sec. II, with the two remaining phases coupling to it. This configuration thus bears a similarity with those of a single line perturbed by lateral branches: here the perturbation would rather be introduced by electromagnetic coupling between multiple conductors. Clearly, in this case it is no longer possible to assume that a shunt fault cuts a line into two separate parts, since aerial and ground modes supported by three-phase lines involve several conductors. The ability of TBM to identify along what phase the fault occurred will not be discussed, since it has already been investigated in EMTR literature [9].

EMTP-RV simulations were setup using a constant-parameter description based on the line cross-section described in Fig. 17, for a soil conductivity of 10 mS/m, with per-unit-length inductance and capacitance matrices

$$L = \begin{bmatrix} 1.76 & 0.83 & 0.86 \\ 0.83 & 1.76 & 0.83 \\ 0.86 & 0.83 & 1.76 \end{bmatrix} \text{mH/km}$$
$$C = \begin{bmatrix} 9.41 & -2.66 & -3.05 \\ -2.66 & 9.10 & -2.66 \\ -3.05 & -2.66 & 9.41 \end{bmatrix} \text{nF/km} \tag{40}$$

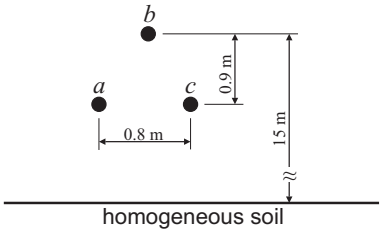

Fig. 17. Cross section of the three-phase overhead line. All conductors have a diameter equal to 18.4 mm.

and a 2 Ω/km per-unit-length resistance for all three conductors. Conduction losses were explicitly included this time, for reasons that will be clarified later. Propagation speeds were found to be equal to 2.99×10^8 m/s for the aerial modes and 2.82×10^8 m/s for the ground mode. The line parameters for the single-phase line involving only phase c, where the fault occurs, were also computed, finding propagation losses with $\alpha = 2.38 \times 10^{-6}$ m^{-1} and a 480 Ω characteristic impedance.

Transfer functions between the fault and the voltages at the left-end of each conductor were computed with EMTP-RV for a line of length $L_T = 10$ km and a fault at distance $L = 6$ km. Fig. 18 shows the transfer functions between the fault and the left end of phase c. Three sets of resonances are superimposed, expected for single-phase lines: a) a 6 km long, relating to the portion of phase c at the left of the fault (black dashed lines), b) a 4 km long for the portion at the right of the fault (blue dashed lines) and c) a 10 km line based on phase a, or equivalently b (red dashed lines). These results are used as references helping to interpret the resonances of the faulty three-phase line. Clearly, it is not suggested that the three-phase line will feature identical resonances: these single-phase results are meant to approximatively identify distinct sources of resonant responses. These resonances were computed from (6b) using propagation speeds for aerial modes for the 10 km line and that for the ground mode for the two lines involving the phase-to-ground fault.

Results in Fig. 18 lead to several conclusions. First, resonances expected if only phase c were present (black dashed lines) accurately represent the resonances of the three-phase line, as long as resonances for the other two sets are not overlap, as for resonances Ⓐ and Ⓑ. Conversely, Ⓒ and Ⓓ, as well as Ⓗ and Ⓘ, are the result of the interaction with resonances with for a 10 km single-phase line (red dashed lines), leading to their splitting along a steeper trajectory, i.e., less sensitive. This phenomenon was already highlighted for a single-junction configuration, and identified as the main mechanism of loss of sensitivity to the fault position. Similarly, resonances for the 4 km portion of phase c (blue dashed lines) lead Ⓖ, Ⓘ and Ⓛ to bend toward them, again with a clear loss of sensitivity at the fault position.

The transfer functions were then processed as explained in the Appendix in order to extract the effective length and spatial resolution of each resonance. These are shown in Fig. 19 for phase c, where it can be seen that the coupling between the three phases results into effective lengths that can be significantly larger than the actual fault distance $L = 6$

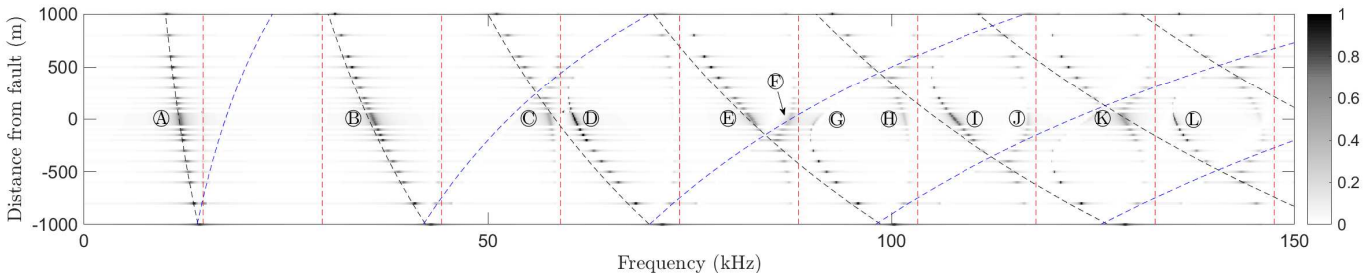

Fig. 18. Resonant response for the three-phase line in Fig. 16 observed from the left end of phase c, for $L_T = 10$ km and $L = 6$ km, as a function of frequency and tested fault position. Dashed lines track the resonance frequencies predicted by (6b) for a single-phase line considering only phase c: a) for the 6 km portion at the left of the fault (black) and b) the 4 km line at its right (blue). Dash-dotted red lines represent the resonance frequencies expected for a 10 km single-phase line, as for phase a, with no fault.

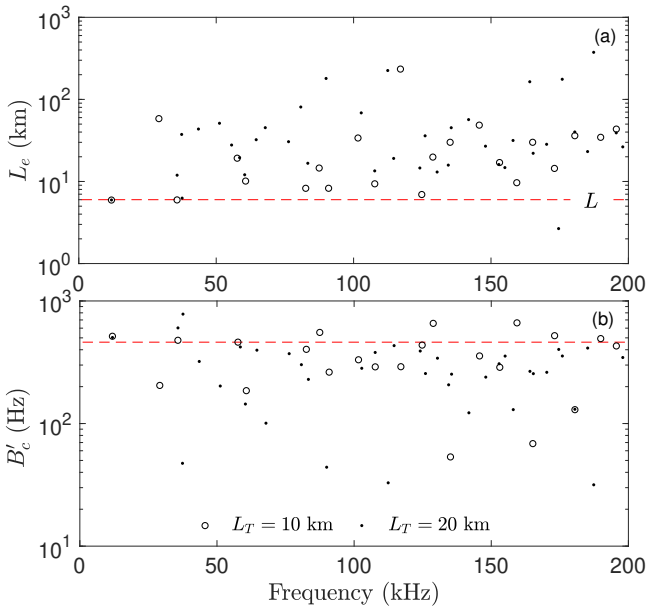

Fig. 19. Effective length (a) and frequency resolution B'_c (b) estimated from simulations of the three-phase line described in Fig. 16, for a probe on phase c.

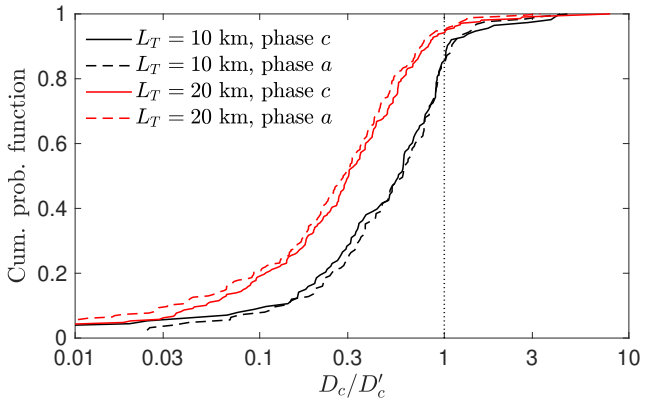

Fig. 20. Empirical cdf of the spatial resolution gain D_c/D'_c for the three-phase line in Fig. 16. Results for probes on phase a and c, computed for a length $L_T = 10$ and 20 km.

km, denoting a loss in sensitivity. The frequency resolution is also affected, but mostly improves with respect to the value of $B_c = 460$ Hz found for the reference single line only involving the portion of phase c at the left of the fault. Hence, also in this case, coupling with the other conductors does not result in equivalent higher losses, which would otherwise systematically result in $B'_c > B_c$.

The gain in spatial resolution with respect to a single line is shown in Fig. 20 and are similar to those reported in Figs. 10 and 13 for one or more lateral branches, apart for a higher statistical dispersion towards values smaller than one. No significant difference was found between the results obtained for the three phases, of which two are reported in Fig. 20. The similarity between these results and those for laterals is not entirely surprising, given the above observations about the loss of sensitivity caused by the interaction between separate resonances.

Propagation losses were explicitly included in this case in order to highlight the role of the portion of line at the right of the fault. When doubling the length of the line to $L_T = 20$ km, the main difference in the results is an increase in the effective length in Fig. 19 and in the spatial resolution loss, in Fig. 20. These effects can be interpreted by noticing how the portion of line after the fault presents resonances of its own, coupled (and thus interfering) with those of the probed left portion. When increasing L_T, propagation losses increase only in the right portion. Their impact can be estimated by computing the loss factor (7) derived for a single line, including propagation losses, which passes from 0.062 for $L_T = 10$ km, to 0.109 for $L_T = 20$ km, for which the spatial resolution would thus be expected to worsen by a factor $0.109/0.062 \simeq 1.76$. This factor closely matches the average ratio between results in Fig. 20 for a 10 and 20 km lines.

It can be concluded that electromagnetic coupling to other conductors leads to a loss of spatial resolution similar to that observed from laterals, explained by a loss of sensitivity to the fault position. The main difference is given by the coupling to the portion of line at the right of the fault, which may increase overall losses, thus affecting the spatial resolution of TBM. It is worth noticing how these conclusions do not necessarily apply to other fault configurations, where more than one conductor would be shunted, potentially resulting in reduced interactions between the pre- and post-fault portions of the line. This would also modify propagation losses, which

strongly depend on the relative excitation of aerial and ground modes.

VI. Conclusion

The spatial resolution of fault-location methods using transient-based methods (TBM) was discussed, explaining the mechanisms behind their potentially super-resolved location, for the case of a single-phase line. The spatial resolution was proven to improve with the degree of resonance of the line, identifying losses as the main parameter controlling spatial resolution of each resonance.

Changes in these results when adding lateral branches were then studied, first theoretically for a single-junction configuration, demonstrating that spatial resolution is degraded because of a loss of sensitivity of the system resonances with respect to the fault position, and not because of higher dissipation, which would have led to a systematic degradation of the frequency resolution. In fact, the latter was rather shown to decrease in a large majority of the resonances. Similar results were found when the number of junctions increases, as well as for a three-phase line, with no evidence of a systematic degradation in the frequency resolution, while a clear loss of sensitivity to the fault position was observed. This phenomenon was shown to occur at frequencies where separate parts of a network or a line would have presented resonances of their own: e.g., fault and lateral branches, or the different conductors of a three-phase line.

Given that the paper highlights that resonance sensitivity to a fault position is a fundamental location mechanism in TBM, this issue should be closely monitored when designing TBM. Numerical simulations are therefore not only necessary to generate reference transients for TBM, but also in design phases in order to estimate their effective location accuracy and potentially filter out resonances that present lower spatial resolution and could thus hamper the overall spatial resolution.

Appendix
Extraction of resonance parameters

The parameters ω_m and τ_m of a resonance can be estimated from the modulus of its frequency response $\psi(\omega;\omega_m,\tau_m)$ by first identifying the angular frequency ω_o where it reaches its peak, for which

$$\omega_o^2 = \omega_m^2 - 1/\tau_m^2. \tag{41}$$

The frequency ω_α at which $|\psi(\omega_\alpha)/\psi(\omega_o)| = \alpha^2$, with $\alpha < 1$, can then be used in order to define a second equation in the two unknown parameters, starting from (8). Applying (41) in this second condition and rearranging it yields

$$\omega_\alpha^2 = \omega_o^2 + 2(\beta/\tau_m)\sqrt{\omega_o^2 + 1/\tau_m^2}, \tag{42}$$

with $\beta = \sqrt{1-\alpha^2}/\alpha$, from which

$$\tau_m^2 = \left(\omega_o^2 + \sqrt{\omega_o^4 + 2a}\right)/a, \tag{43}$$

where $a = (\omega_\alpha^2 - \omega_o^2)^2/2\beta^2$. The coherence bandwidth B_c of the resonant response is then obtained from (14).

The sensitivity $S(\omega_m)$ of a resonance to the fault position is found as in (15), approximated by a numerical derivative that requires running simulations not only at the actual fault position L, but also $L \pm \delta x$, where $\delta x \ll L$. The effective length is then given by $L_e = \omega_m/2\pi S(\omega)$, following its definition in (29), while the spatial resolution is found as $D_c(\omega_m) = B_c/S(\omega_m)$.

References

[1] P. A. Crossley and P. G. McLaren, "Distance protection based on travelling waves," *IEEE Trans. Power App. Syst.*, vol. PAS-102, no. 9, pp. 2971–2983, Sep. 1983.

[2] G. B. Ancell and N. C. Pahalawaththa, "Maximum likelihood estimation of fault location on transmission lines using travelling waves," *IEEE Trans. Power Del.*, vol. 9, no. 2, pp. 680–689, April 1994.

[3] Z. Q. Bo, G. Weller, and M. A. Redfern, "Accurate fault location technique for distribution system using fault-generated high-frequency transient voltage signals," *IEE Proceedings - Generation, Transmission and Distribution*, vol. 146, no. 1, pp. 73–79, Jan 1999.

[4] R. Stevens and T. Stringfield, "A transmission line fault locator using fault-generated surges," *Trans. Amer. Inst. of Electrical Engineers*, vol. 67, no. 2, pp. 1168–1179, 1948.

[5] M. Aurangzeb, P. A. Crossley, and P. Gale, "Fault location on a transmission line using high frequency travelling waves measured at a single line end," in *2000 IEEE Power Engineering Society Winter Meeting. Conference Proceedings (Cat. No.00CH37077)*, vol. 4, Jan 2000, pp. 2437–2442 vol.4.

[6] M. Farshad and J. Sadeh, "A novel fault-location method for HVDC transmission lines based on similarity measure of voltage signals," *IEEE Trans. Power Del.*, vol. 28, no. 4, pp. 2483–2490, Oct 2013.

[7] F. Deng, X. Li, and X. Zeng, "Single-ended travelling wave protection algorithm based on full waveform in the time and frequency domains," *IET Gener. Transm. Distrib*, vol. 12, no. 15, pp. 3680–3691, 2018.

[8] M. Smail, L. Pichon, M. Olivas, F. Auzanneau, and M. Lambert, "Detection of defects in wiring networks using time domain reflectometry," *Trans. Magn.*, vol. 46, no. 8, pp. 2998–3001, 2010.

[9] R. Razzaghi, G. Lugrin, H. Manesh, C. Romero, M. Paolone, and F. Rachidi, "An efficient method based on the electromagnetic time reversal to locate faults in power networks," *IEEE Trans. Power Del.*, vol. 28, no. 3, pp. 1663–1673, 2013.

[10] S. He, A. Cozza, and Y. Xie, "Electromagnetic time reversal as a correlation estimator: Improved metrics and design criteria for fault location in power grids," *IEEE Trans. Electromagn. Compat.*, in press.

[11] R. Razzaghi, G. Lugrin, F. Rachidi, and M. Paolone, "Assessment of the influence of losses on the performance of the electromagnetic time reversal fault location method," *IEEE Trans. Power Del.*, vol. 32, no. 5, pp. 2303–2312, Oct 2017.

[12] Z. Wang, S. He, Q. Li, B. Liu, R. Razzaghi, M. Paolone, Y. Xie, M. Rubinstein, and F. Rachidi, "A full-scale experimental validation of electromagnetic time reversal applied to locate disturbances in overhead power distribution lines," *IEEE Trans. Electromagn. Compat.*, vol. 60, no. 5, pp. 1562–1570, Oct 2018.

[13] G. W. Swift, "The spectra of fault-induced transients," *IEEE Trans. Power App. Syst.*, vol. PAS-98, no. 3, pp. 940–947, May 1979.

[14] A. Borghetti, M. Bosetti, C. A. Nucci, M. Paolone, and A. Abur, "Integrated use of time-frequency wavelet decompositions for fault location in distribution networks: Theory and experimental validation," *IEEE Trans. Power Del.*, vol. 25, no. 4, pp. 3139–3146, Oct 2010.

[15] L. U. Iurinic, R. G. Ferraz, and A. S. Bretas, "Characteristic frequency of travelling waves applied for transmission lines fault location estimation," in *2013 IEEE Grenoble Conference*, June 2013, pp. 1–5.

[16] T. Gonen, *Electrical power transmission system engineering: analysis and design*. CRC press, 2015.

[17] R. E. Collin, *Foundations for microwave engineering*. McGraw-Hill, 1966.

[18] A. Cozza, S. He, and Y. Xie, "Impact of propagation losses on fault location accuracy in full transient-based methods," *IEEE Trans. Power Del.*, under review.

[19] L. Cohen, *Time-frequency analysis: theory and applications*. Prentice-Hall, Inc., 1995.

[20] M. M. Saha, J. J. Izykowski, and E. Rosolowski, *Fault location on power networks*. Springer Science & Business Media, 2009.

[21] A. Greenwood, *Electrical transients in power systems*. John Wiley and Sons Inc., New York, USA, 1991.